

# Hyperspectral Anomaly Detection With Attribute and Edge-Preserving Filters

Xudong Kang, *Senior Member, IEEE*, Xiangping Zhang, Shutao Li, *Senior Member, IEEE*,  
 Kenli Li, *Senior Member, IEEE*, Jun Li, *Senior Member, IEEE*,  
 and Jón Atli Benediktsson, *Fellow, IEEE*

**Abstract**—A novel method for anomaly detection in hyperspectral images is proposed. The method is based on two ideas. First, compared with the surrounding background, objects with anomalies usually appear with small areas and distinct spectral signatures. Second, for both the background and the objects with anomalies, pixels in the same class are usually highly correlated in the spatial domain. In this paper, the pixels with specific area property and distinct spectral signatures are first detected with attribute filtering and a Boolean map-based fusion approach in order to obtain an initial pixel-wise detection result. Then, the initial detection result is refined with edge-preserving filtering to make full use of the spatial correlations among adjacent pixels. Compared with other widely used anomaly detection methods, the experimental results obtained on real hyperspectral data sets including airport, beach, and urban scenes demonstrate that the performance of the proposed method is quite competitive in terms of computing time and detection accuracy.

**Index Terms**—Anomaly detection, attribute filtering, Boolean map, edge-preserving filtering, hyperspectral image.

## I. INTRODUCTION

HYPERSPECTRAL imagery provides a wealth of spectral information in remotely sensed scenes via hundreds of spectral bands. Through analyzing hyperspectral images, it is possible to distinguish different objects of interest based on their spectral signatures, and thus, hyperspectral imaging is a well-suited tool for various remote sensing applications

Manuscript received December 19, 2016; revised April 6, 2017 and May 15, 2017; accepted May 24, 2017. Date of publication July 27, 2017; date of current version September 25, 2017. This paper was supported in part by the National Natural Science Foundation of China under Grant 61601179, in part by the National Natural Science Fund of China for Distinguished Young Scholars under Grant 61325007, in part by the National Natural Science Fund of China for International Cooperation and Exchanges under Grant 61520106001, and in part by the Science and Technology Plan Projects Fund of Hunan Province under Project 2015WK3001. (*Corresponding author: Shutao Li*.)

X. Kang, X. Zhang, and S. Li are with the College of Electrical and Information Engineering, Hunan University, Changsha 410082, China (e-mail: shutao\_li@hnu.edu.cn).

K. Li is with the College of Information Science and Engineering, National Supercomputing Center in Changsha, Hunan University, Changsha 410082, China.

J. Li is with the Guangdong Provincial Key Laboratory of Urbanization and Geo-simulation, Center of Integrated Geographic Information Analysis, School of Geography and Planning, Sun Yat-sen University, Guangzhou 510275, China.

J. A. Benediktsson is with the Faculty of Electrical and Computer Engineering, University of Iceland, 101 Reykjavik, Iceland.

Color versions of one or more of the figures in this paper are available online at <http://ieeexplore.ieee.org>.

Digital Object Identifier 10.1109/TGRS.2017.2710145

such as scene classification, spectral unmixing, and target detection [1]–[3]. Among these applications, hyperspectral anomaly detection has drawn a lot of attention due to its importance in military and civilian applications [4]–[6].

Given a hyperspectral image, the goal of hyperspectral anomaly detection is to identify the interesting targets that look quite different spatially or spectrally from its surroundings. For example, ships in a sea background and tanks in a forest background can be referred to as anomalies. Such a problem is usually treated as detecting outliers with reference to a model of the background. To achieve this objective, statistical modeling and geometrical modeling are two widely used strategies for most current anomaly detection algorithms.

Statistical models used for anomaly detection are most often related to the Gaussian distribution due to its mathematical tractability. For example, the well-known Reed–Xiaoli (RX) detector [7] is based on a multivariate Gaussian model characterizing the background information. Specifically, the background statistical model is first constructed by estimating the mean and covariance values of the samples in the whole image (or a local window around the test pixel). Then, the anomalies are detected by calculating the Mahalanobis distance between each test pixel and the statistical model. In addition to the classical RX detector, several variants of the RX algorithm have also been proposed. For example, a kernel RX algorithm is proposed in [8], which takes into account the higher order relationships between the spectral bands by mapping the hyperspectral data into a high-dimensional feature space that could be potentially of infinite dimension. Another successful Gaussian model-based anomaly detection method is the cluster-based anomaly detection (CBAD) method [9]. Instead of constructing the background model using all pixels or pixels in a local window, the CBAD method first segments the scene into different clusters that are spectrally homogeneous and then detects anomalies in each cluster. One disadvantage of the above mentioned methods is that they use statistics from a contaminated data set, which means that background statistics actually contain anomalies. To address this issue, several anomaly detection algorithms have been proposed in recent researches, such as the random-selection-based anomaly detector [10], weighted RX detector [11], discriminative metric learning-based anomaly detector [12], and robust no-linear anomaly detector [13]. For example, the random selection-based anomaly detector randomly selects image pixels multiple times to construct the background statistics so as to

effectively avoid contamination of the background statistics by anomaly pixels.

Instead of estimating statistical models for the background, geometrical modeling-based methods assume that background pixels can be approximately represented by a group of major spectra or bases extracted from the image, while anomalies cannot. The subspace-based method [14] is one of the most popular geometrical modeling-based anomaly detection methods. In [14], the background is assumed to be laying in a low-dimensional subspace that is constructed by a set of bases that are acquired by a linear transformation, e.g., the singular value decomposition. Through projecting the pixels to the background orthogonal subspace, the representation residual of each pixel is calculated for anomaly detection. Based on a similar idea, sparse representation- and tensor representation-based anomaly detection methods have also been researched in recent years [15]–[17]. In [17], the hyperspectral image is first represented with a three-order tensor composed of a core tensor and three factor matrices, in which the major and minor principal components (PCs) of the three factor matrices correspond to the background and the anomaly information, respectively. Then, a reconstruction-error-based method is used to find the largest PCs to eliminate the background information as much as possible, and thus, the anomalies can be easily detected in the remaining data. Since the spatial locations of different pixels are well incorporated in the tensor representation, this paper demonstrates that spatial information also has an important role in anomaly detection, which has not been well studied in previous research works. In [16], the anomalies are determined from the residual image that is obtained by subtracting the predicted background (each pixel in the background is approximately sparsely represented by its spatial neighborhoods) from the original hyperspectral image. In [18], the background spectral signal is assumed to be stable and slowly varying. In view of this point, an interesting slowly varying background analysis-based method is used to estimate the background signals based on the original data and the differential image.

Different from previous works, this paper uses local filtering operations, i.e., attribute and edge preserving for the objective of anomaly detection. First, a characteristic image is first extracted from the hyperspectral data using the PC analysis method, which is optimal for data representation in the mean square sense. Without this step, the proposed method is also expected to be useful in multispectral anomaly detection applications. Then, one of the most prominent spectral–spatial hyperspectral image description methods, i.e., morphological attribute filtering [19], and a Boolean map-based fusion method are used to extract the anomaly candidates with specific area properties. Finally, in order to further decrease false alarms in the detection result, edge-preserving filtering [20] is adopted for postprocessing of the initial detection result, in which the local spatial correlations among adjacent pixels are well employed. In addition to a widely used real hyperspectral data set, a novel hyperspectral anomaly detection data set captured at different scenes is constructed in this paper. Experiments performed on three real hyperspectral data sets demonstrate the effectiveness of the

proposed method in terms of detection accuracy and computing time.

The rest of this paper is organized as follows. The attribute and edge-preserving filters (EPFs) are reviewed in Section II. The proposed attribute and edge-preserving filtering-based anomaly detection (AED) method is introduced in Section III. The experimental results are given in Section IV. Finally, conclusions are given in Section V.

## II. BACKGROUND

### A. Attribute Filtering

Morphological attribute thinnings and thickenings (referred to attribute filters) are morphological adaptive filters introduced in [21]. In recent years, attribute filters have been successfully applied in the hyperspectral image classification field [19], [22]. The advantage of attribute filtering is that it could effectively represent the spatial structures in the hyperspectral image by preserving or removing the connected components in the image according to predefined attribute predicates. Here, we will briefly describe the principle of attribute filters. For a complete description of the morphological attribute filter and its applications in hyperspectral image classification, we refer the reader to [19].

Specifically, given a grayscale image  $\mathbf{I}$ , with values ranging from 0 to  $Z$ . Its lower and upper level sets,  $E$ , can be defined as  $\{\mathbf{I} \leq t\}$  and  $\{\mathbf{I} \geq t\}$ , respectively, in which  $t \in 0, 1, \dots, Z$ . Therefore, the lower level set  $\{\mathbf{I} \leq t\} \subseteq E$  actually refers to a set of Boolean maps obtained by thresholding an image at all possible values of its pixels. Similarly, the upper level set is also a set of Boolean maps obtained according to  $\mathbf{I} \geq t$ . The lower and upper level sets,  $E$ , are composed of the connected components ( $CC \subseteq E$ ), which are usually referred as peak components. Attribute filtering is performed to these peak components, using a predefined logical predicate  $T_\kappa^\alpha$ , in which the attribute  $\alpha$  computed on  $CC$  is compared against a threshold  $\kappa$ . For example,  $T_{50}^{\text{area}}$  actually compares the area of  $CC$  with 50. If the area of  $CC$  is smaller than 50 pixels, the outcome of  $T_\kappa^\alpha(CC)$  will be “false”. In this situation, the connected component  $CC$  will be removed from the image. However, if the area of  $CC$  is larger than 50 pixels, the connected component  $CC$  will be preserved in the image. The attribute filtering performed on the upper and lower sets is called as attribute thinning and thickening, respectively. Furthermore, besides the “area” attribute, other attributes can also be used to define the logical predicate  $T_\kappa^\alpha$ , such as “standard deviation”, “moment of inertia”, and so on. The outputs of attribute filtering are computed by processing all the connected components present in the lower or upper level sets ( $CC \subseteq E$ ) according to the defined logical predicate  $T_\kappa^\alpha$ .

Although attribute filter was proposed almost two decades ago, it has not been well applied in remote sensing applications in part due to its high computing cost. In recent years, that problem has been addressed by decomposing the image with a tree-based representation [23]. Specifically, the connected components of a grayscale image can be represented in a max-tree (alternatively, min-tree) through their inclusion relations. In this situation, the input image can be represented as a rooted

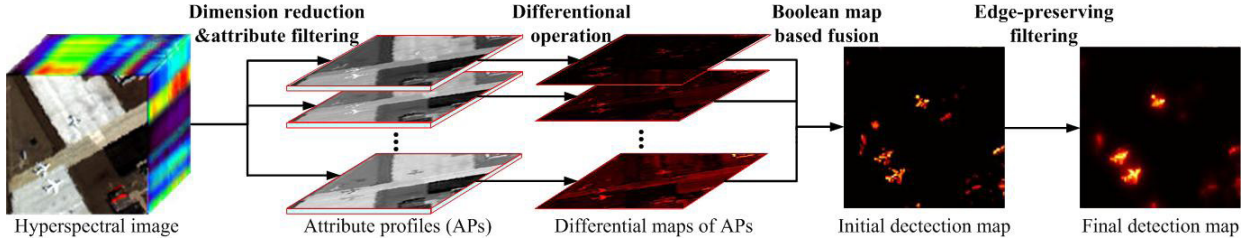


Fig. 1. Schematic of the proposed attribute filtering and edge-preserving filtering-based anomaly detection method.

tree of peak components, and thus, the filtering process can be modeled as a node or branch removal process. The advantage of the tree-based representation is that each tree needs to be computed only once, and then multiple filtering outputs can be derived from it.

### B. Edge-Preserving Filtering

Edge-preserving filtering is a filtering technique to smooth images while preserving edges, which having received considerable attention from the research community over the last two decades [24]–[26]. In recent years, edge-preserving filtering has been applied successfully in remote sensing applications such as hyperspectral feature extraction and image classification [27]–[29]. For example, in [27], edge-preserving filtering is applied for the postprocessing of classification results obtained by a support vector machine classifier, in which edge-preserving filtering is demonstrated to be an effective way in making full use of the local spatial information of hyperspectral images. Based on a similar idea, in this paper, edge-preserving filtering is adopted for anomaly detection in hyperspectral images.

The most popular filters in the edge-preserving filtering class are the bilateral filter [30] and anisotropic diffusion [31]. The disadvantages of the two filters are that they are originally designed with high computing cost. Specifically, bilateral filter uses a space-varying weighting function computed at a space of higher dimensionality than the signal being filtered, while anisotropic diffusion requires an iterative solution. Although several techniques have been proposed to accelerate anisotropic diffusion or bilateral filtering, these methods may rely on approximate operations, or natively only handle grayscale images [32]–[34]. Furthermore, many different EPFs, e.g., the guided filter [24], and the domain transform filters [20] have been proposed as alternatives ways of edge-preserving filtering. Among these filters, the domain transform recursive filter is a real-time EPF and has been demonstrated to have stable performances in terms of computing time and filtering quality [20]. Therefore, the domain transform recursive filter is adopted in this paper.

Given a 1-D signal, domain transform recursive filter first applies a distance-preserving transform to the input signal. Although a perfect distance-preserving transformation does not exist, a simple approximation is the sum of the spatial distance (e.g., one pixel distance) and intensity difference between every two pixels. Specifically, let  $I$  denote the input signal, the transformed signal  $U$  can be calculated

as follows:

$$U_i = I_0 + \sum_{j=1}^i \left( 1 + \frac{\delta_s}{\delta_r} |I_j - I_{j-1}| \right) \quad (1)$$

where  $\delta_s$  and  $\delta_r$  are two additional parameters to adjust the amount of smoothness in filtering. The input signal  $I$  is then processed by recursive filtering as follows:

$$J_i = (1 - a^b)I_i + a^b J_{i-1} \quad (2)$$

where  $J_i$  is the filter output of the  $i$ th pixel,  $a = \exp [(-\sqrt{2}/\delta_s)] \in [0, 1]$  is a feedback coefficient, and  $b$  is the distance between neighbor samples  $U_i$  and  $U_{i-1}$  in the transform domain. As  $b$  increases,  $a^b$  goes to zero, which stops the propagation chain and, thus, edges will be preserved, and vice versa.

Domain transform recursive filter processes images using the above-mentioned 1-D operations by performing separate passes along each dimension of the image. In [20], it has been demonstrated that artifact-free filtered images can be obtained by performing 1-D filtering iteratively (more than three iterations).

As shown in (1) and (2), the domain transform recursive filter accumulates the image gradients to measure the distance  $b$  between two pixels. Instead of measuring this distance using the input image, another type of edge-preserving filtering, i.e., joint edge-preserving filtering, can be constructed by using another input image as guidance. Specifically, let  $G$  denote the guidance image.  $G_i$  is the value at pixel  $i$  of the guidance image. Equation (1) can be modified as follows:

$$U_i = G_0 + \sum_{j=1}^i \left( 1 + \frac{\delta_s}{\delta_r} |G_j - G_{j-1}| \right). \quad (3)$$

Therefore, in this paper, we refer the filtered image with  $DTRF(I, G, \delta_s, \delta_r)$  for the domain transform recursive filtering (DTRF), in which  $I$  represents the input image,  $G$  refers to the guidance image that is used to compute the distance  $b$  in (2), and  $\delta_s$  and  $\delta_r$  refer to the parameters of the filter to adjust the amount of smoothness in filtering.

### III. PROPOSED APPROACH

Fig. 1 shows the schematic diagram of the proposed method, which consists of the following steps. First, the attribute profiles (APs) of the hyperspectral image are obtained with dimension reduction and attribute filtering. Then, through calculating the differences among the APs and performing

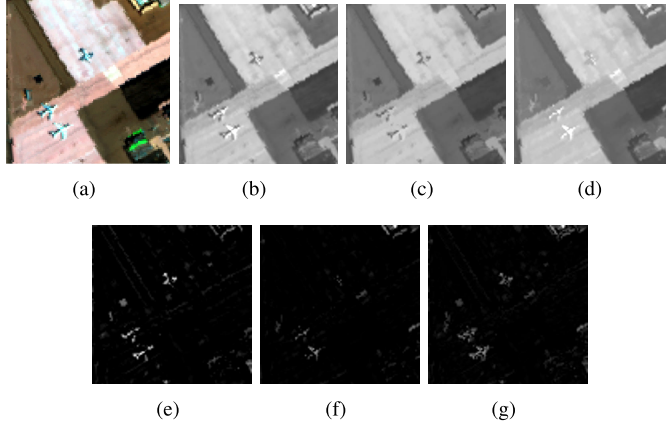


Fig. 2. False color composite of the (a) hyperspectral image, (b) first PC, and the APs obtained with (c) attribute thinning and (d) thickening opening, respectively.

a Boolean map based fusion, an initial detection map is obtained. Finally, edge-preserving filtering is used as a post-processing step to obtain the final detection map.

#### A. Image Decomposition With Attribute Filters

Given a hyperspectral image  $\mathbf{f}$ , the spectral dimension of  $\mathbf{f}$  is first reduced to  $M$  by performing PC analysis on the hyperspectral data. The PC analysis method is adopted since it is optimal for data representation in the mean square sense. The influence of the dimension  $M$  on the detection performance will be analyzed in the experiments. Then, given a predefined logical predicate  $T_\kappa^a$ , let  $\hat{\mathbf{f}}$  represent the dimension reduced image, and let  $\gamma$  and  $\phi$  denote, respectively, the attribute thinnings and thickenings, the APs of the dimension reduced hyperspectral image can be constructed as follows:

$$AF(\hat{\mathbf{f}}_m) = \{\gamma(\hat{\mathbf{f}}_m), \phi(\hat{\mathbf{f}}_m)\}. \quad (4)$$

In real remote sensing scenes, anomaly objects in hyperspectral images usually appear as small-area objects compared with the background. Although this assumption is quite simple and intuitive, it is actually not well considered by previous researches in this field. To make full use of the area information of different objects, in this paper, area serves as the predefined logical predicate, and thus,  $T_\kappa^a$  is set to be  $T_\kappa^{area}$  and the influence of the parameter  $\kappa$  will be analyzed in Section IV.

Fig. 2 shows an example of attribute filtering with  $\kappa$  set as 25. Given a hyperspectral image captured at San Diego Airport [see Fig. 2(a)], we calculate the APs of its first PC. Fig. 2(b)–(d) shows the first PC of the hyperspectral image and the resulting APs. It can be seen that, with the attribute thinning and thickening operations, the bright [see Fig. 2(c)] and dark [see Fig. 2(d)] connected components with area  $\leq 25$  have been removed from the first PC of the hyperspectral image.

#### B. Differential Map Computation and Fusion

The objective of the above-mentioned attribute filtering step is to remove the connected bright (thinning operation) and dark

(thickening operation) components in the image with specific area property, i.e., area  $\leq \kappa$ . In order to detect these small-area objects, the differential and fusion stage consists of the following steps.

First, a simple differential operation is adopted to calculate the differences among the attribute filtered images and the original image

$$\mathbf{s}_m = |\phi(\hat{\mathbf{f}}_m) - \hat{\mathbf{f}}_m| + |\hat{\mathbf{f}}_m - \gamma(\hat{\mathbf{f}}_m)| = \phi(\hat{\mathbf{f}}_m) - \gamma(\hat{\mathbf{f}}_m) \quad (5)$$

where  $\mathbf{s}_m$  is the  $m$ th differential map [see Fig. 2(g)], which refers to the probabilities that bright objects [i.e.,  $|\hat{\mathbf{f}}_m - \gamma(\hat{\mathbf{f}}_m)|$ , see Fig. 2(e)] and dark objects [i.e.,  $|\phi(\hat{\mathbf{f}}_m) - \hat{\mathbf{f}}_m|$ , see Fig. 2(f)] in the  $m$ th PC of the hyperspectral image. Since  $\phi(\hat{\mathbf{f}}_m) \geq \hat{\mathbf{f}}_m$  and  $\hat{\mathbf{f}}_m \geq \gamma(\hat{\mathbf{f}}_m)$  are always satisfied for each image pixel, the original image can be removed, and thus the differential map  $\mathbf{s}_m$  can be directly calculated as  $\phi(\hat{\mathbf{f}}_m) - \gamma(\hat{\mathbf{f}}_m)$ , which is shown in Fig. 2(g).

Then, to further penalize background objects with large areas, each differential map is processed as follows:

$$\hat{\mathbf{s}}_m^i = \begin{cases} \mathbf{s}_m^i & \text{if } \mathbf{B}_m^i == 1 \\ 0 & \text{Otherwise.} \end{cases} \quad (6)$$

Here  $\mathbf{B}$  is a set of Boolean maps obtained by thresholding the dilated differential maps

$$\mathbf{B}_m = \text{AERO\_FILTERING}(\text{THRESH}(\mathbf{s}_m \oplus \mathcal{K}_\omega, \theta), \lambda). \quad (7)$$

Here, the function  $\text{THRESH}(\cdot, \theta)$  assigns 1 to a pixel if its value in the input map is greater than  $\theta$ , and 0 otherwise.  $\theta$  is chosen with the widely used Otsu's method [35] due to its robust performance in image binarization. The function  $\text{AERO\_FILTERING}(\cdot, \lambda)$  assigns 0 to pixels in a connected component if its area is greater than  $\lambda$  pixels. When  $\lambda$  is very large, this step actually has no influence to the detection performance. However, when  $\lambda$  is very small, background and anomaly objects may be all removed from the detection map, and thus, decrease the detection accuracy. In this paper, the optimal value for  $\lambda$  is set to be  $N/100$ , in which  $N$  is the number of pixels in the hyperspectral image.  $\mathcal{K}_\omega$  is a square dilation kernel of width  $\omega = 2$ .  $\oplus$  represents the dilation operation.

Finally, the postprocessed differential maps are fused together to obtain an initial anomaly detection map

$$\mathbf{d} = \frac{\sum_m^M \hat{\mathbf{s}}_m}{M}. \quad (8)$$

#### C. Postprocessing With Edge-Preserving Filtering

In this stage, the initial detection map obtained above is refined with DTRF as follows:

$$\hat{\mathbf{d}} = \text{DTRF}(\mathbf{d}, \mathbf{g}, \delta_s, \delta_r) \quad (9)$$

where the function DTRF refers to the DTRF operation and  $\mathbf{g}$  is a color image constructed by the first three PCs of the hyperspectral image, which serves as the guidance image for DTRF.  $\delta_s$  and  $\delta_r$  are two parameters that control the smoothness of the filtering output.  $\hat{\mathbf{d}}$  is the resulting anomaly detection map.

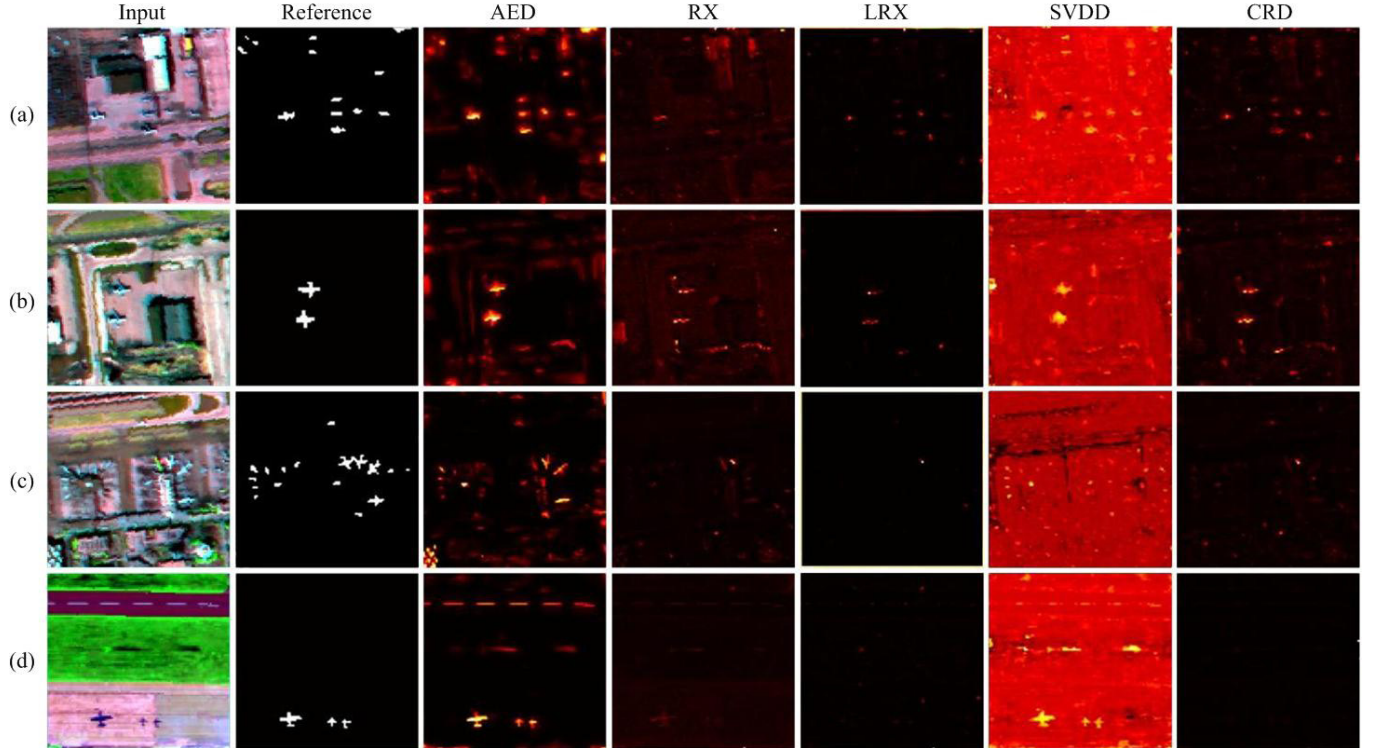


Fig. 3. Color composites of hyperspectral images (airport scene) and detection maps of the compared methods. The second column shows the reference detection maps, which are obtained by human labeling.

The advantage of this postprocessing step is that the spatial information in hyperspectral images is considered in the filtering process. Specifically, in the filtering process, instead of measuring the distance  $b$  in (2) using the initial detection map,  $b$  is measured according to the  $l_1$ -norm distance between those pixels in the dimension reduced hyperspectral image  $\mathbf{g}$ . This joint filtering operation ensures that neighboring pixels that have similar pixel values in  $\mathbf{g}$  tend to have similar values in the final detection map. The motivation is that, for both background and anomaly objects, pixels belonging to the same object are usually highly correlated in the spatial domain (generally, neighboring pixels with similar pixel values can be considered as spatially highly correlated).

#### IV. EXPERIMENTS

##### A. Data Sets

In this section, the proposed method is evaluated on two real hyperspectral data sets captured at different scenes, which are listed as follows.

1) *Airport–Beach–Urban (ABU) Data Set*: The first and second columns of Figs. 3–5 show the sample images and reference detection maps in the ABU data set. The sample images of size  $100 \times 100$  are manually extracted from large images downloaded from the Airborne Visible/Infrared Imaging Spectrometer (AVIRIS) Web site.<sup>1</sup> Furthermore, noisy bands in the original images have been removed using a recently published noisy level estimation method [36]. The reference maps of the sample images are manually labeled with the help of the Environment for Visualizing

TABLE I  
SOME FEATURES OF THE ABU DATA SET  
Airport Scene (Fig. 3)

Images	Captured place	Resolution	Sensor	Fight time
(a)	Los Angeles	7.1m	AVIRIS	11/9/2011
(b)	Los Angeles	7.1m	AVIRIS	11/9/2011
(c)	Los Angeles	7.1m	AVIRIS	11/9/2011
(d)	Gulfport	3.4m	AVIRIS	7/7/2010

Beach Scene (Fig. 4)

Images	Captured place	Resolution	Sensor	Fight time
(a)	Cat Island	17.2m	AVIRIS	9/12/2010
(b)	San Diego	7.5m	AVIRIS	11/16/2011
(c)	Bay Champagne	4.4m	AVIRIS	7/4/2010
(d)	Pavia	1.3m	ROSIS-03	Unknown

Urban Scene (Fig. 5)

Images	Captured place	Resolution	Sensor	Fight time
(a)	Texas Coast	17.2m	AVIRIS	8/29/2010
(b)	Texas Coast	17.2m	AVIRIS	8/29/2010
(c)	Gainesville	3.5m	AVIRIS	9/4/2010
(d)	Los Angeles	7.1m	AVIRIS	11/9/2011
(e)	Los Angeles	7.1m	AVIRIS	11/9/2011

Images (ENVI) software. Some features of these images are listed in Table I. As shown in Table I, most of the images are captured by the AVIRIS sensor except Fig. 4(d), which is captured by the Reflective Optics System Imaging Spectrometer (ROSIS-03) sensor. Moreover, due to the different heights of the flights, the spatial resolutions of the images are also different. The ABU data set has been made available on the first author's homepage.<sup>2</sup>

<sup>1</sup><http://aviris.jpl.nasa.gov/>

<sup>2</sup><http://xudongkang.weebly.com/>

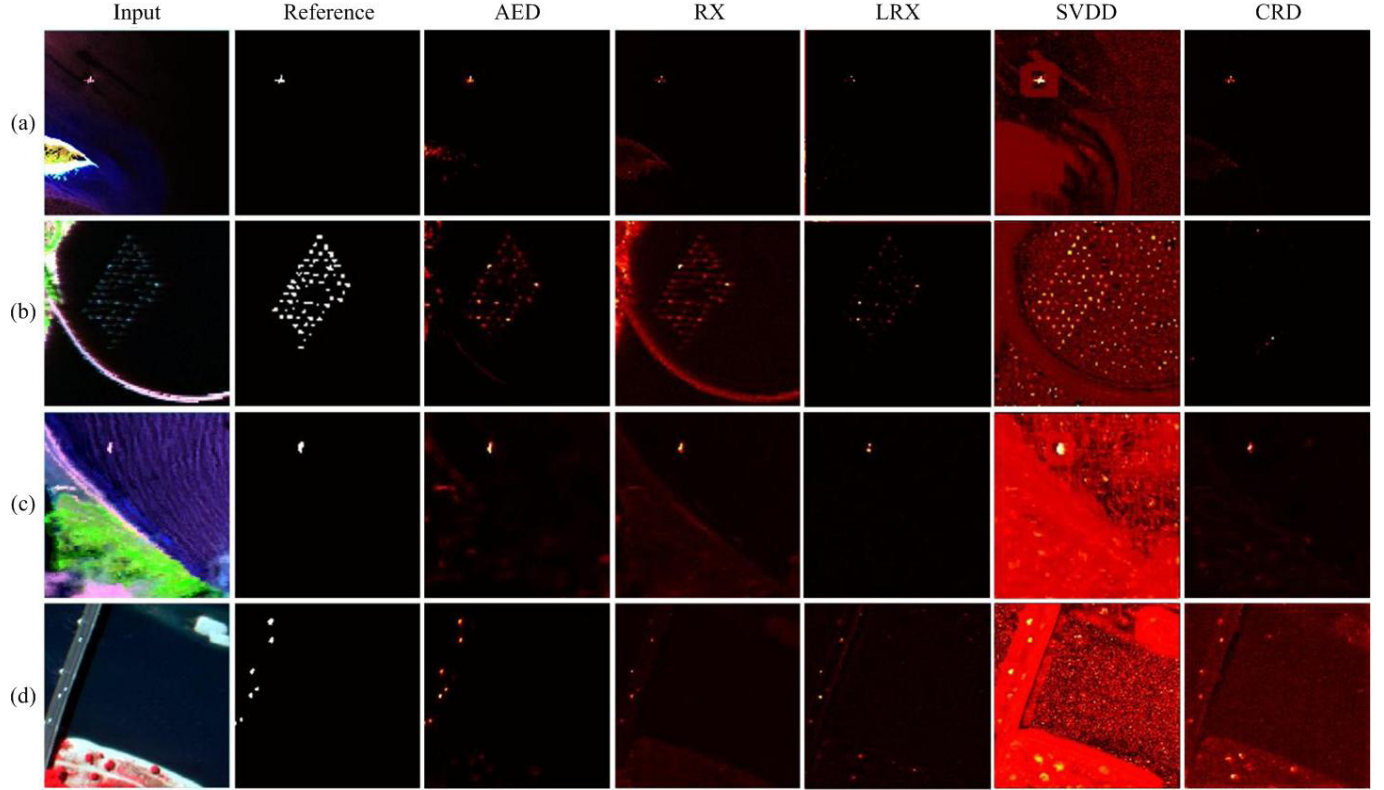


Fig. 4. Color composites of hyperspectral images (beach scene) and detection maps of the compared methods. The second column shows the reference detection maps, which are obtained by human labeling.

2) *San Diego Data Set*: The second data set used in the experiments has been widely used in related publications. It was captured by the AVIRIS sensor over the San Diego airport area, CA, USA. This image is of size  $100 \times 100 \times 189$ , in which the noisy bands have been removed. The two aircrafts are regarded as the anomaly objects in the image. The sample image and reference detection map for this data set are shown in Fig. 6(a) and (b), respectively.

3) *HYDICE Data Set*: The third data set was captured by the Hyperspectral Digital Imagery Collection Experiment (HYDICE) sensor over an urban area, CA, USA. The image is of size  $80 \times 100 \times 175$ , in which the noisy bands have been removed. The ground truth of this data set includes 21 anomalous pixels, which are cars and roofs. The sample image and reference detection map for this data set are shown in Fig. 7(a) and (b), respectively.

#### B. Detection Performance

In this section, the anomaly detection performance of the proposed AED is evaluated. In the experiments, four widely used anomaly detection methods, i.e., the RX detector [7], local RX (LRX) detector [7], support vector data description (SVDD) [37], and collaborative representation-based detector (CRD) [16], are used for comparison. These methods are either frequently cited in the literature or have leading performances on several real hyperspectral data sets.

One of the most widely used metric for anomaly detection evaluation is the receiver operating characteristic (ROC) area under the curve (AUC) metric [38]. Specifically, given a detection map and a reference map, the AUC value is calculated

as follows:

$$\text{AUC} = \int_{-\infty}^{+\infty} \text{TPR}(H)\text{FPR}'(H)dH \quad (10)$$

where true positive rate  $\text{TPR}(H)$  defines how many correct positive results occur among all positive samples, when the threshold for the detection map is set as  $H$ . FPR, on the other hand, defines how many incorrect positive results occur among all negative samples available. The advantage of the AUC metric is that it depends only on the order of the pixels rather than absolute detection values. Therefore, AUC is adopted in this paper to evaluate the objective performances of different methods. Furthermore, as suggested in [39], ROC curves and confidence intervals are also used in this paper for objective evaluation.

Experiments are performed on the ABU, San Diego, and HYDICE data sets. In order to generate the results reported in Figs. 3–7, the optimal parameters of the LRX, SVDD, and CRD methods are selected for each sample image according to the corresponding AUC performances. For example, it is known that the detection performance of local anomaly detectors is sensitive to the window size ( $\omega_{in}$  and  $\omega_{out}$ ). By varying  $\omega_{in}$  from 3 to 19 and  $\omega_{out}$  from 5 to 23, the optimal window size for each local anomaly detector could be selected based on the AUC metric. Similarly, the  $\sigma$  parameter of the SVDD method is also selected using a similar way by varying the value of  $\sigma$  from 1 to 40. Furthermore, for the CRD method, since it has been demonstrated that the performance is insensitive to the regularization parameter  $\lambda$ , this parameter is fixed as  $10^{-6}$  in our experiments as suggested in [16].

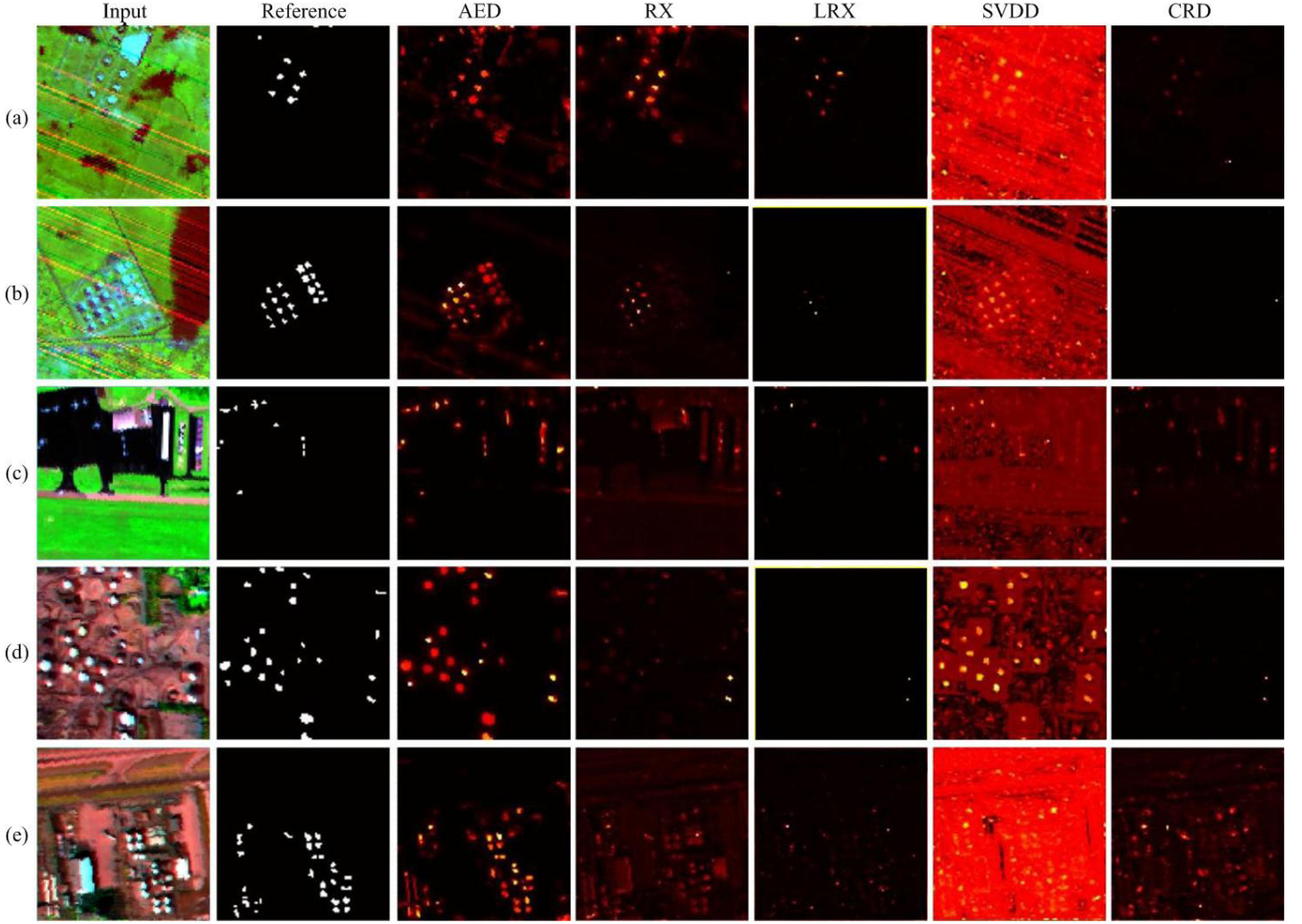


Fig. 5. Color composites of hyperspectral images (urban scene) and detection maps of the compared methods. The second column shows the reference detection maps, which are obtained by human labeling.

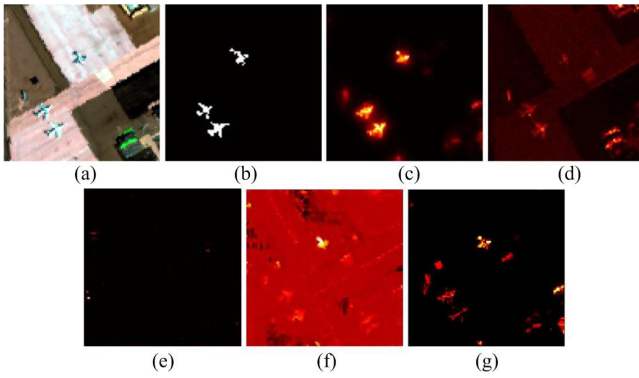


Fig. 6. Color composite of the (a) San Diego image, (b) reference detection map, and the detection maps of the (c) AED method, (d) RX method, (e) LRX method, (f) SVDD method, and (g) CRD method.

For the proposed method, a default parameter setting  $\kappa = 25$ ,  $\sigma_s = 5$ ,  $\sigma_r = 0.5$ ,  $M = 3$  is adopted for most of sample images, which will be analyzed detailedly in the next part of this section. This default parameter setting cannot obtain the best performances for all sample images, while providing stable and acceptable performances for most of sample images.

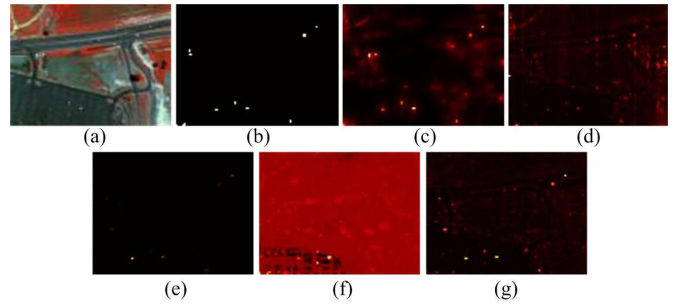


Fig. 7. Color composite of the (a) HYDICE image, (b) reference detection map, and the detection maps of the (c) AED method, (d) RX method, (e) LRX method, (f) SVDD method, and (g) CRD method.

Furthermore, for several sample images that contain anomaly objects of relatively large or small scales, the threshold  $\kappa$  also needs to be adjusted. Specifically, as shown in Figs. 3(b) and (d) and 5(c), since the area of anomaly objects in these images are much larger than those in other images, the  $\kappa$  parameter is set as  $\kappa = 64$  for the three data sets. In contrast,  $\kappa = 5$  is adopted for the HYDICE data set since the objects in this image are usually appeared as isolated pixels. Finally, the parameter  $\sigma_r$  has also been adjusted to

TABLE II  
EVALUATION SCORES ON THE ABU AND SAN DIEGO DATA SETS

ABU-Airport Scene (Fig. 3)					
Images	AED	RX [7]	LRX [7]	SVDD [37]	CRD [16]
a	<b>0.9923</b>	0.8221	0.9458	0.9501	0.9577
b	<b>0.9936</b>	0.8404	0.9874	0.9900	0.9744
c	<b>0.9756</b>	0.9288	0.9467	0.9080	0.9564
d	<b>0.9953</b>	0.9526	0.8740	0.9848	0.9757
Avg.	<b>0.9892</b>	0.8859	0.9384	0.9582	0.9660

ABU-Beach Scene (Fig. 4)					
Images	AED	RX [7]	LRX [7]	SVDD [37]	CRD [16]
a	<b>0.9974</b>	0.9807	0.9956	0.9583	0.9916
b	<b>0.9825</b>	0.9106	0.9777	0.9620	0.9416
c	0.9997	<b>0.9999</b>	0.9997	<b>0.9999</b>	0.9996
d	<b>0.9973</b>	0.9538	0.9391	0.9561	0.9450
Avg.	<b>0.9942</b>	0.9613	0.9780	0.9691	0.9695

ABU-Urban Scene (Fig. 5)					
Images	AED	RX [7]	LRX [7]	SVDD [37]	CRD [16]
a	<b>0.9980</b>	0.9907	0.9968	0.9862	0.9948
b	<b>0.9985</b>	0.9946	0.9231	0.9356	0.9410
c	<b>0.9976</b>	0.9513	0.9800	0.9658	0.9634
d	<b>0.9912</b>	0.9887	0.9696	0.9621	0.9816
e	<b>0.9845</b>	0.9692	0.9538	0.9449	0.9521
Avg.	<b>0.9940</b>	0.9789	0.9647	0.9589	0.9666

San Diego Airport (Fig. 6)					
Image	AED	RX [7]	LRX [7]	SVDD [37]	CRD [16]
a	<b>0.9850</b>	0.9403	0.8656	0.9710	0.9746

HYDICE (Fig. 7)					
Image	AED	RX [7]	LRX [7]	SVDD [37]	CRD [16]
a	<b>0.9951</b>	0.9857	0.9890	0.9897	0.9727

$\sigma_r = 1$  for the San Diego and HYDICE data sets so as to obtain the most optimal detection performances on the two widely used data sets. For each method, the AUC scores are presented in Table II. The best scores are emphasized in bold for each image. As shown in Table II, the AED method achieves the best scores on most of the hyperspectral images except it ranks as second for Fig. 4(c). According to the order of Figs. 3–5, the average AUCs obtained by the proposed AED method are 0.9892, 0.9942, and 0.9940, which are much higher than those obtained by the second best approach in each case, 0.9660 (CRD method), 0.9780 (LRX method), and 0.9789 (RX method). For the San Diego data set (Fig. 6), the AUC score, i.e.,  $AUC = 0.9850$ , obtained by the proposed AED method is also the highest. Although the performance of CRD is relatively stable, it does not in any case provide the best AUC scores. The CRD method in most cases shows better performances than the RX method, which is consistent with the results reported in [16]. We also compare the ROC curves and point-wise confidence intervals [39] of different methods on two sample images, i.e., Figs. 3(c) and 5(c). As shown in Fig. 8, the proposed method always exhibits higher true positive rates when the false positive rate varies from 0 to 1 ( $\log_2$  coordinate is used). Furthermore, the point-wise confidence intervals (the bootstrap-based confidence bound estimation method<sup>3</sup> is implemented by `perfcurve.m`) of different

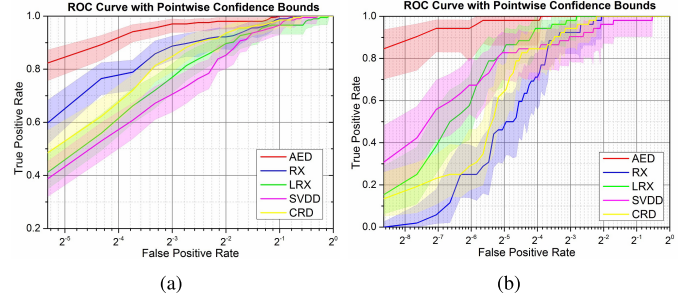


Fig. 8. ROC curves and confidence intervals for Figs. 3(c) and 5(c).

methods are also shown in Fig. 8. It can be seen that the proposed AED offers a better result than all other detection methods since its confidence bounds are always higher than others when TPR varies from 0 to 1.

The sample images and detection maps of compared methods are shown in Figs. 3–6. By examining the detection maps visually, we find that AED tends to be less attracted by high contrast edge areas and can better highlight the anomaly objects of different sizes, even though it does not involve multiscale processing. For example, in Fig. 4(b), the anomaly objects in the ocean area can be well detected by the AED and RX methods. However, the RX method tends to emphasize the strong edge area in this example, and thus, decreasing its detection accuracy. The SVDD and CRD methods usually have stable detection performances, while they may emphasize background signals for some sample images, such as Fig. 4(d). When compared with other anomaly detection methods, the major advantage of the proposed method is its robust detection performances in different scenes. Taking Fig. 3 for example, the proposed method can detect the airplanes in all sample images. Moreover, the shapes of the anomaly objects are also very clear in our detection results since the edge-preserving filtering operation could make full use of the spatial correlations among adjacent pixels. By contrast, the RX method performs not well in this airport scene. As shown in Fig. 3(b), although the RX method can detect the positions of the two airplanes, the shape of the airplane is still missing. More importantly, for Fig. 3(a), (c), and (d), most of the airplanes in the scene are not able to be detected by the RX method. The reported average AUC scores on the ABU-Airport data set ( $AUC = 0.9923$  and  $0.8221$  for the AED and RX methods, respectively) also support this observation. In general, the detection maps are consistent with the AUC values reported in Table II, and thus, it is able to conclude that the AED method shows competitive performances for hyperspectral anomaly detection.

The speed of different methods is also compared on a computer with 2.8-GHz CPU and 8-GB memory. We measure the speed of all methods on the San Diego data set, where the size of the input image is  $100 \times 100 \times 189$ . All methods are implemented in MATLAB and the computing time recorded in seconds is shown in Table III. As shown in Table III, the MATLAB implementation of the proposed anomaly detection method is very fast, taking about 0.27 s for the San Diego data set. Furthermore, since the attribute and edge-preserving

<sup>3</sup><https://se.mathworks.com/help/stats/perfcurve.html>

TABLE III

COMPUTING TIME (SECONDS) OF DIFFERENT METHODS ON THE SAN DIEGO DATA SET

Methods	AED	RX [7]	LRX [7]	SVDD [37]	CRD [16]
Time	0.27	<b>0.12</b>	40.31	377.55	39.25

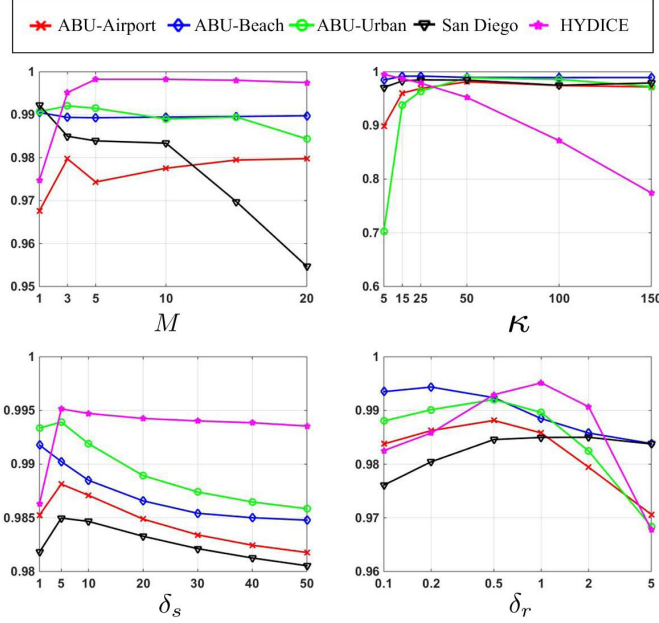


Fig. 9. Effects of the parameters,  $M$ ,  $\kappa$ ,  $\delta_s$ , and  $\delta_r$  over the average AUCs of AED on each data set.

filtering operations both have real-time implementations in a GPU environment [20], [40], the application of the proposed AED method in a real anomaly detection application will be a relatively easy task.

### C. Parameter and Component Analysis

This section first analyzes the influence of different parameters on the performance of the proposed AED method. These parameters include the band number,  $M$ , of the dimension reduced data, the thresholding number,  $\kappa$ , of the attribute filter, and the parameters of the DTRF, i.e.,  $\delta_s$  and  $\delta_r$ , which control the smoothness of the filtering output. Here, the area under the ROC curves (AUC) is used to evaluate the objective performances of the proposed method under different parameter settings. Fig. 9 shows the effects of the parameters,  $M$ ,  $\kappa$ ,  $\delta_s$ , and  $\delta_r$  over the average AUCs of AED on each data set. When analyzing one of the parameters, the other parameters will be fixed as a default parameter setting  $M = 3$ ,  $\kappa = 25$ ,  $\delta_s = 5$ , and  $\delta_r = 0.5$ . As shown in the top left of Fig. 9, it can be first seen that when the number of dimensions  $M$  is greater than three, the AUCs of AED tend to be stable and may decrease dramatically for the HYDICE data set. As shown in the top right of Fig. 9, when  $\kappa$  is quite small, the detection accuracy will be quite low since objects with area larger than  $\kappa$  will be hard to be detected. Furthermore, when  $\kappa$  is quite large, some false anomaly objects may be detected, and thus, decreasing the AUC scores. The bottom subfigures shows the influence

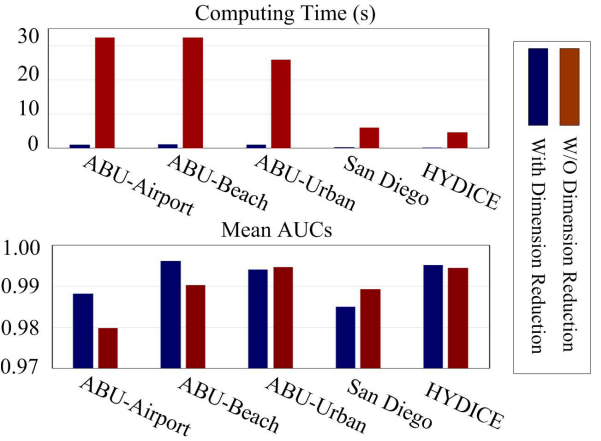


Fig. 10. Total computing time and average AUC scores of AED with and without the dimension reduction step.

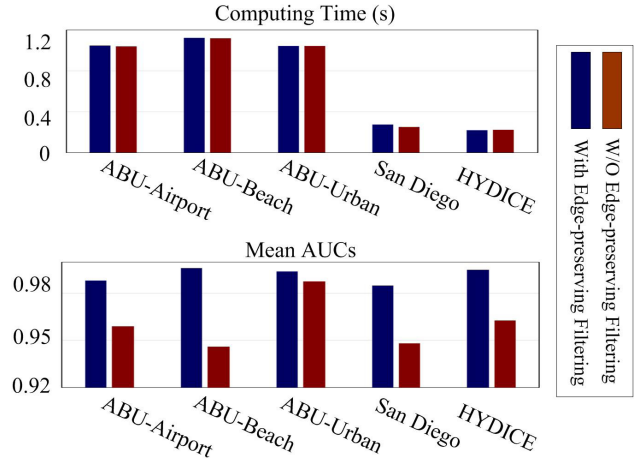


Fig. 11. Total computing time and average AUC scores of AED with and without the edge-preserving filtering step.

of  $\delta_s$  and  $\delta_r$  on the detection performance. As shown in the two subfigures, the optimal  $\delta_s$  and  $\delta_r$  for the ABU data set should be  $\delta_s = 5$  and  $\delta_r = 0.5$ . However, for the San Diego and HYDICE data set, the optimal  $\delta_s$  and  $\delta_r$  should be  $\delta_s = 5$  and  $\delta_r = 1$ .

Then, we analyze the effects of two major preprocessing and postprocessing components, i.e., the dimension reduction and edge-preserving filtering steps, over the average AUCs of AED on each data set. We show in Fig. 10 the computing time and average AUC scores of AED with and without dimension reduction. It can be seen that the computing time of AED can be extremely reduced with the dimension reduction step, while the AUC scores of the AED method will not be influenced seriously. For example, for the ABU-Airport, ABU-Beach, and HYDICE data sets, the dimension reduction step can even help little on the AUC scores. We show in Fig. 11 the computing time and average AUC scores of AED with and without the edge-preserving filtering step. It can be observed that the edge-preserving filtering step is actually very efficient. Furthermore, the edge-preserving filtering step plays a very important role in improving the detection performances, especially for

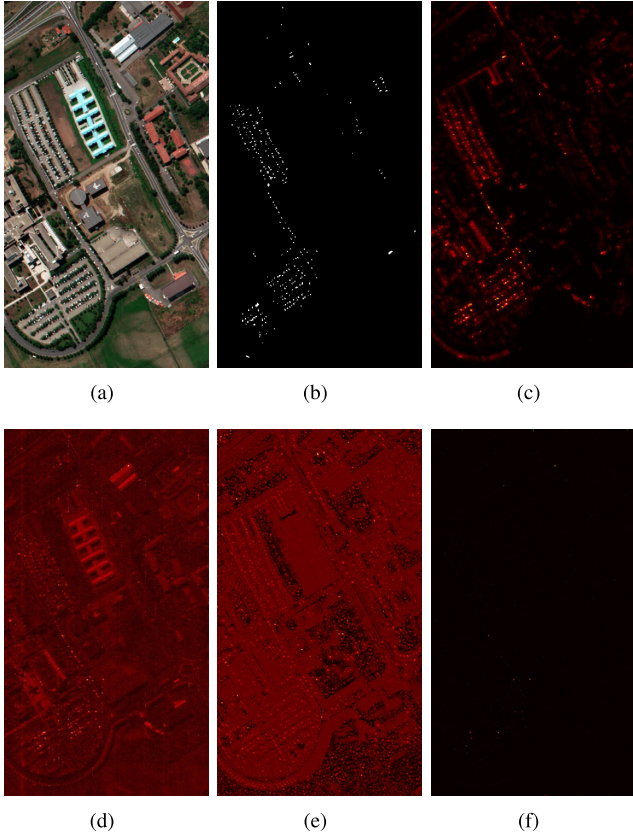


Fig. 12. Detection maps obtained by different methods on the University of Pavia data set. False color composite of the (a) hyperspectral image, (b) reference detection map, and the detection maps of the (c) AED method, (d) RX method, (e) SVDD method, and (f) CRD method. The results of the RX and CRD methods have been enhanced using a logarithm transform for visualization. The result of the LRX is not presented since its result looks quite similar to the one obtained by the CRD method.

the ABU-airport, ABU-Beach, San Diego, and HYDICE data sets. This observation demonstrates that the spatial information indeed helps a lot in anomaly detection. Considering that most of existing anomaly detection methods have not well considered the spatial correlations among adjacent pixels in the detection process, how to combine spectral and spatial information with other advancing tools such as graph model and manifold learning will be an interesting future research topic.

#### D. Application of the AED Detector in Vehicle Detection

In this section, the University of Pavia data set is used to further demonstrate the application of the proposed method for vehicle detection in images of larger sizes or contain complex scenes. The University of Pavia data set has a spatial dimension of  $610 \times 340$  and 115 spectral bands, which is much larger than those used in previous experiments (most of previous experiments are performed on images of  $100 \times 100$  pixels). A three-band false color image and the reference detection map are presented in Fig. 12. As shown in Fig. 12(a) and (b), the scene contains a number of vehicles in the parks and roads, which can be considered as anomalies in this scene. More importantly, the background of this scene

TABLE IV  
EVALUATION SCORES ON THE UNIVERSITY OF PAVIA DATA SET

Methods	AED	RX [7]	LRX [7]	SVDD [37]	CRD [16]
AUC	<b>0.9911</b>	0.9414	0.9486	0.9530	0.9522
Time (s)	4.1	<b>2.2</b>	425.4	5398.3	547.7

is relatively complex, and thus, can be considered as a more challenging data set compared with the data sets used in previous experiments.

In this experiment, the parameters of the proposed method is fixed as  $\kappa = 25$ ,  $\sigma_s = 5$ ,  $\sigma_r = 0.5$ , and  $M = 3$ . The parameters of the other compared methods are selected optimally according to performance of AUC. Fig. 12 and Table IV show the detection maps and corresponding AUC scores obtained by different methods. It can be seen that the proposed method is able to highlight the vehicles in this scene and achieves the highest AUC score, i.e., AUC = 0.9911. More importantly, the computing time of the proposed method is also very competitive. It takes only 4.15 s for processing the University of Pavia data set. By contrast, the LRX, SVDD, and CRD methods are all quite time consuming, and thus, hard to be used in real applications. The RX method is very efficient while it is not able to highlight the vehicles in the detection result.

## V. CONCLUSION

In this paper, a novel attribute and edge-preserving filtering-based algorithm is proposed for anomaly detection in hyperspectral images. The proposed method consists of two stages, i.e., attribute filtering-based initial detection and edge-preserving filtering-based postprocessing. The advantage of attribute filtering is that it can effectively extract objects with specific area properties in a hyperspectral image. The proposed edge-preserving filtering-based postprocessing is important in the proposed AED method, since it can make full use of the local spatial information in the anomaly detection process. The experimental results reported in this paper show that the proposed AED method is able to obtain outstanding detection performances on several real hyperspectral data sets captured from different scenes. However, it should be mentioned that the empirically parameter setting method is one limitation of the proposed detector when it is applied in real application. How to automatically decide the optimal parameters for the proposed method will be the focus of our future work.

## ACKNOWLEDGEMENT

The authors would like to thank Prof. W. Li for providing the code of the CRD method and Dr. N. Falco for discussing about the design of the proposed method.

## REFERENCES

- [1] A. Plaza *et al.*, “Recent advances in techniques for hyperspectral image processing,” *Remote Sens. Environ.*, vol. 113, pp. S110–S122, Sep. 2009.
- [2] R. Heylen, M. Parente, and P. Gader, “A review of nonlinear hyperspectral unmixing methods,” *IEEE J. Sel. Topics Appl. Earth Observ. Remote Sens.*, vol. 7, no. 6, pp. 1844–1868, Jun. 2014.

- [3] X. Kang, S. Li, L. Fang, M. Li, and J. A. Benediktsson, "Extended random walker-based classification of hyperspectral images," *IEEE Trans. Geosci. Remote Sens.*, vol. 53, no. 1, pp. 144–153, Jan. 2015.
- [4] D. Manolakis and G. S. Shaw, "Detection algorithms for hyperspectral imaging applications," *IEEE Signal Process. Mag.*, vol. 19, no. 1, pp. 29–43, Jan. 2002.
- [5] D. W. J. Stein, S. G. Beaven, L. E. Hoff, E. M. Winter, A. P. Schaum, and A. D. Stocker, "Anomaly detection from hyperspectral imagery," *IEEE Signal Process. Mag.*, vol. 19, no. 1, pp. 58–69, Jan. 2002.
- [6] C.-I. Chang and S.-S. Chiang, "Anomaly detection and classification for hyperspectral imagery," *IEEE Trans. Geosci. Remote Sens.*, vol. 40, no. 6, pp. 1314–1325, Jun. 2002.
- [7] I. S. Reed and X. Yu, "Adaptive multiple-band CFAR detection of an optical pattern with unknown spectral distribution," *IEEE Trans. Acoust., Speech Signal Process.*, vol. 38, no. 10, pp. 1760–1770, Oct. 1990.
- [8] H. Kwon and N. M. Nasrabadi, "Kernel RX-algorithm: A nonlinear anomaly detector for hyperspectral imagery," *IEEE Trans. Geosci. Remote Sens.*, vol. 43, no. 2, pp. 388–397, Feb. 2005.
- [9] M. J. Carlotto, "A cluster-based approach for detecting man-made objects and changes in imagery," *IEEE Trans. Geosci. Remote Sens.*, vol. 43, no. 2, pp. 374–387, Feb. 2005.
- [10] B. Du and L. Zhang, "Random-selection-based anomaly detector for hyperspectral imagery," *IEEE Trans. Geosci. Remote Sens.*, vol. 49, no. 5, pp. 1578–1589, May 2011.
- [11] Q. Guo, B. Zhang, Q. Ran, L. Gao, J. Li, and A. Plaza, "Weighted-RXD and linear filter-based RXD: Improving background statistics estimation for anomaly detection in hyperspectral imagery," *IEEE J. Sel. Topics Appl. Earth Observ. Remote Sens.*, vol. 7, no. 6, pp. 2351–2366, Jun. 2014.
- [12] B. Du and L. Zhang, "A discriminative metric learning based anomaly detection method," *IEEE Trans. Geosci. Remote Sens.*, vol. 52, no. 11, pp. 6844–6857, Nov. 2014.
- [13] R. Zhao, B. Du, and L. Zhang, "A robust nonlinear hyperspectral anomaly detection approach," *IEEE J. Sel. Topics Appl. Earth Observ. Remote Sens.*, vol. 7, no. 4, pp. 1227–1234, Apr. 2014.
- [14] K. I. Ranney and M. Soumekh, "Hyperspectral anomaly detection within the signal subspace," *IEEE Geosci. Remote Sens. Lett.*, vol. 3, no. 3, pp. 312–316, Jul. 2006.
- [15] J. Li, H. Zhang, L. Zhang, and L. Ma, "Hyperspectral anomaly detection by the use of background joint sparse representation," *IEEE J. Sel. Topics Appl. Earth Observ. Remote Sens.*, vol. 8, no. 6, pp. 2523–2533, Jun. 2015.
- [16] W. Li and Q. Du, "Collaborative representation for hyperspectral anomaly detection," *IEEE Trans. Geosci. Remote Sens.*, vol. 53, no. 3, pp. 1463–1474, Mar. 2015.
- [17] X. Zhang, G. Wen, and W. Dai, "A tensor decomposition-based anomaly detection algorithm for hyperspectral image," *IEEE Trans. Geosci. Remote Sens.*, vol. 54, no. 10, pp. 5801–5820, Oct. 2016.
- [18] R. Zhao, B. Du, L. Zhang, and L. Zhang, "Beyond background feature extraction: An anomaly detection algorithm inspired by slowly varying signal analysis," *IEEE Trans. Geosci. Remote Sens.*, vol. 54, no. 3, pp. 1757–1774, Mar. 2016.
- [19] M. Dalla Mura, J. A. Benediktsson, B. Waske, and L. Bruzzone, "Morphological attribute profiles for the analysis of very high resolution images," *IEEE Trans. Geosci. Remote Sens.*, vol. 48, no. 10, pp. 3747–3762, Oct. 2010.
- [20] E. S. L. Gastal and M. M. Oliveira, "Domain transform for edge-aware image and video processing," *ACM Trans. Graph.*, vol. 30, no. 4, pp. 69:1–69:12, 2011.
- [21] E. J. Breen and R. Jones, "Attribute openings, thinnings, and granulometries," *Comput. Vis. Image Understand.*, vol. 64, no. 3, pp. 377–389, Nov. 1996.
- [22] P. Ghamisi, M. Dalla Mura, and J. A. Benediktsson, "A survey on spectral-spatial classification techniques based on attribute profiles," *IEEE Trans. Geosci. Remote Sens.*, vol. 53, no. 5, pp. 2335–2353, May 2015.
- [23] P. Salembier, A. Oliveras, and L. Garrido, "Antiextensive connected operators for image and sequence processing," *IEEE Trans. Image Process.*, vol. 7, no. 4, pp. 555–570, Apr. 1998.
- [24] K. He, J. Sun, and X. Tang, "Guided image filtering," *IEEE Trans. Pattern Anal. Mach. Intell.*, vol. 35, no. 6, pp. 1397–1409, Jun. 2013.
- [25] B. Sun, S. Li, and J. Sun, "Scanned image descreening with image redundancy and adaptive filtering," *IEEE Trans. Image Process.*, vol. 23, no. 8, pp. 3698–3710, Aug. 2014.
- [26] G. Tereece, "The bitonic filter: Linear filtering in an edge-preserving morphological framework," *IEEE Trans. Image Process.*, vol. 25, no. 11, pp. 5199–5211, Nov. 2016.
- [27] X. Kang, S. Li, and J. A. Benediktsson, "Spectral-spatial hyperspectral image classification with edge-preserving filtering," *IEEE Trans. Geosci. Remote Sens.*, vol. 52, no. 5, pp. 2666–2677, May 2014.
- [28] X. Kang, S. Li, and J. A. Benediktsson, "Feature extraction of hyperspectral images with image fusion and recursive filtering," *IEEE Trans. Geosci. Remote Sens.*, vol. 52, no. 6, pp. 3742–3752, Jun. 2014.
- [29] J. Xia, L. Bombrun, T. Adali, Y. Berthoumieu, and C. Germain, "Spectral-spatial classification of hyperspectral images using ICA and edge-preserving filter via an ensemble strategy," *IEEE Trans. Geosci. Remote Sens.*, vol. 54, no. 8, pp. 4971–4982, Aug. 2016.
- [30] C. Tomasi and R. Manduchi, "Bilateral filtering for gray and color images," in *Proc. IEEE Int. Conf. Comput. Vis.*, Jan. 1998, pp. 839–846.
- [31] P. Perona and J. Malik, "Scale-space and edge detection using anisotropic diffusion," *IEEE Trans. Pattern Anal. Mach. Intell.*, vol. 12, no. 7, pp. 629–639, Jul. 1990.
- [32] J. Chen, S. Paris, and F. Durand, "Real-time edge-aware image processing with the bilateral grid," *ACM Trans. Graph.*, vol. 26, no. 3, p. 103, Jul. 2007.
- [33] A. Criminisi, T. Sharp, C. Rother, and P. Pérez, "Geodesic image and video editing," *ACM Trans. Graph.*, vol. 29, no. 5, pp. 134:1–134:15, 2010.
- [34] Q. Yang, K.-H. Tan, and N. Ahuja, "Real-time O(1) bilateral filtering," in *Proc. IEEE Int. Conf. Comput. Vis. Pattern Recognit.*, Jun. 2009, pp. 557–564.
- [35] N. Otsu, "A threshold selection method from gray-level histograms," *Automatica*, vol. 11, nos. 285–296, pp. 23–27, 1975.
- [36] X. Liu, M. Tanaka, and M. Okutomi, "Single-image noise level estimation for blind denoising," *IEEE Trans. Image Process.*, vol. 22, no. 12, pp. 5226–5237, Dec. 2013.
- [37] A. Banerjee, P. Burlina, and C. Diehl, "A support vector method for anomaly detection in hyperspectral imagery," *IEEE Trans. Geosci. Remote Sens.*, vol. 44, no. 8, pp. 2282–2291, Aug. 2006.
- [38] C. Ferri, J. Hernández-Orallo, and P. Flach, "A coherent interpretation of AUC as a measure of aggregated classification performance," in *Proc. Int. Conf. Mach. Learn.*, 2011, pp. 657–664.
- [39] J. Kerekes, "Receiver operating characteristic curve confidence intervals and regions," *IEEE Geosci. Remote Sens. Lett.*, vol. 5, no. 2, pp. 251–255, Apr. 2008.
- [40] J. M. Molero, E. M. Garzón, I. García, E. S. Quintana-Ortí, and A. Plaza, "Efficient implementation of hyperspectral anomaly detection techniques on GPUs and multicore processors," *IEEE J. Sel. Topics Appl. Earth Observ. Remote Sens.*, vol. 7, no. 6, pp. 2256–2266, Jun. 2014.



**Xudong Kang** (S'13–M'15–SM'17) received the B.Sc. degree from Northeast University, Shenyang, China, in 2007, and the Ph.D. degree from Hunan University, Changsha, China, in 2015.

From 2012 to 2013 and 2016 to 2017, he was a Visiting Scholar in electrical engineering with the University of Iceland, Reykjavik, Iceland. In 2015, he joined the College of Electrical Engineering, Hunan University. His research interests include hyperspectral feature extraction, image classification, data fusion, and anomaly detection.

Dr. Kang was a recipient of the second prize in the Student Paper Competition held at the 2014 IEEE International Geoscience and Remote Sensing Symposium, Quebec. He serves as a reviewer for a number of journals, including the IEEE TRANSACTIONS ON GEOSCIENCE AND REMOTE SENSING, the IEEE TRANSACTIONS ON IMAGE PROCESSING, and so on. He was also selected as the Best Reviewer for the IEEE GEOSCIENCE AND REMOTE SENSING LETTERS in 2016.



**Xiangping Zhang** received the B.Sc. degree from Shandong University, Jinan, China, in 2014. She is currently pursuing the M.S. degree in electrical engineering with Hunan University, Changsha, China.

Her research interests include hyperspectral image anomaly detection.



**Jun Li** (M'12–SM'16) received the B.S. degree in geographic information systems from Hunan Normal University, Changsha, China, in 2004, the M.E. degree in remote sensing from Peking University, Beijing, China, in 2007, and the Ph.D. degree in electrical engineering from the Instituto de Telecomunicações, Instituto Superior Técnico (IST), Universidade Técnica de Lisboa, Lisbon, Portugal, in 2011.

From 2007 to 2011, she was a Marie Curie Research Fellow with the Departamento de Engenharia Electrotécnica e de Computadores and the Instituto de Telecomunicações, IST, where she was involved in the framework of the European Doctorate for signal processing. She has also been actively involved in the hyperspectral imaging network, which is a Marie Curie Research Training Network involving 15 partners in 12 countries and is intended to foster research, training, and cooperation on hyperspectral imaging at the European level. Since 2011, she has been a Post-Doctoral Researcher with the Hyperspectral Computing Laboratory, Department of Technology of Computers and Communications, Escuela Politécnica, University of Extremadura, Cáceres, Spain. She is currently a Professor with Sun Yat-sen University, Guangzhou, China. Her research interests include hyperspectral image classification and segmentation, spectral unmixing, signal processing, and remote sensing.

Dr. Li has been a reviewer for several journals, including the IEEE TRANSACTIONS ON GEOSCIENCE AND REMOTE SENSING, the IEEE GEOSCIENCE AND REMOTE SENSING LETTERS, *Pattern Recognition*, *Optical Engineering*, the *Journal of Applied Remote Sensing*, and *Inverse Problems and Imaging*. She is an Associate Editor of the IEEE JOURNAL OF SELECTED TOPICS IN APPLIED EARTH OBSERVATIONS AND REMOTE SENSING.



**Shutao Li** (M'07–SM'15) received the B.S., M.S., and Ph.D. degrees in electrical engineering from Hunan University, Changsha, China, in 1995, 1997, and 2001, respectively.

In 2001, he joined the College of Electrical and Information Engineering, Hunan University. In 2001, he was a Research Associate with the Department of Computer Science, Hong Kong University of Science and Technology, Hong Kong, where he was a Visiting Professor in 2005. From 2002 to 2003, he was a Post-Doctoral Fellow with the Royal Holloway College, University of London, Surrey, U.K. He is currently a Full Professor with the College of Electrical and Information Engineering, Hunan University. He is also a Chang-Jiang Scholar Professor appointed by the Ministry of Education of China. He has authored or co-authored more than 180 refereed papers. His research interests include compressive sensing, sparse representation, image processing, and pattern recognition.

Dr. Li was an Editorial Board Member of the Information Fusion, Sensing, and Imaging. He was a recipient of two Second-Grade National Awards at the Science and Technology Progress of China in 2004 and 2006. In 2013, he was a recipient of the National Science Fund for Distinguished Young Scholars in China. He is an Associate Editor of the IEEE TRANSACTIONS ON GEOSCIENCE AND REMOTE SENSING and the IEEE TRANSACTIONS ON INSTRUMENTATION AND MEASUREMENT.



**Jón Atli Benediktsson** (S'84–M'90–SM'99–F'04) received the Cand.Sci. degree in electrical engineering from the University of Iceland, Reykjavík, Iceland, in 1984, and the M.S.E.E. and Ph.D. degrees in electrical and computer engineering from Purdue University, West Lafayette, IN, USA, in 1987 and 1990, respectively.

He is currently the Rector and a Professor of Electrical and Computer Engineering with the University of Iceland. He is a Co-founder of the biomedical startup company, Oxymap. His research interests include remote sensing, biomedical analysis of signals, pattern recognition, image processing, and signal processing. He has authored extensively in these fields.

Prof. Benediktsson is a member of the Association of Chartered Engineers in Iceland (VFI), Societas Scinetiarum Islandica, and Tau Beta Pi. He is a fellow of SPIE. He was a recipient of the S. J. Kristof Award from Purdue University in 1991 as an Outstanding Graduate Student in remote sensing, the Icelandic Research Council's Outstanding Young Researcher Award in 1997, the IEEE Third Millennium Medal in 2000, the yearly Research Award from the Engineering Research Institute, University of Iceland, in 2006, the Outstanding Service Award from the IEEE GEOSCIENCE AND REMOTE SENSING SOCIETY (GRSS) in 2007, and the 2013 IEEE/VFI Electrical Engineer of the Year Award in 2007. He was a co-recipient of the 2012 IEEE TRANSACTIONS ON GEOSCIENCE AND REMOTE SENSING (TGRS) Paper Award, the IEEE GRSS Highest Impact Paper Award, and the University of Iceland's Technology Innovation Award in 2004. He is on the International Editorial Board of the *International Journal of Image and Data Fusion*. He was the 2011–2012 President of the IEEE GRSS and has been on the GRSS Administrative Committee since 2000. He was an Editor of the IEEE TGRS from 2003 to 2008, and has been an Associate Editor of the IEEE TGRS since 1999. He has been an Associate Editor of the IEEE GEOSCIENCE AND REMOTE SENSING LETTERS since 2003 and the IEEE ACCESS since 2013. He was the Chairman of the Steering Committee of the IEEE JOURNAL OF SELECTED TOPICS IN APPLIED EARTH OBSERVATIONS AND REMOTE SENSING from 2007 to 2010.



**Kenli Li** (SM'15) received the Ph.D. degree in computer science from the Huazhong University of Science and Technology, Wuhan, China, in 2003.

He is currently a Full Professor of Computer Science and Technology with Hunan University, Changsha, China. He has authored more than 150 papers in international conferences and journals, such as the IEEE TRANSACTIONS ON COMPUTERS, the IEEE TRANSACTIONS ON PARALLEL AND DISTRIBUTED SYSTEMS, and the *Journal of Parallel and Distributed Computing*. His research interests include parallel computing and cloud computing.

Dr. Li is an Outstanding Member of CCF. He is currently on the Editorial Board of the IEEE TRANSACTIONS ON COMPUTERS.